Bulletin of the Seismological Society of America, Vol. 96, No. 4B, pp. S269–S282, September 2006, doi: 10.1785/0120050818

Ⓔ

Coseismic and Postseismic Slip of the 2004 Parkfield Earthquake from Space-Geodetic Data

by Ingrid A. Johanson,* Eric J. Fielding, Frederique Rolandone, and Roland Bürgmann

Abstract We invert interferometric synthetic aperture radar (InSAR) data jointly with campaign and continuous global positioning system (GPS) data for slip in the coseismic and postseismic periods of the 2004 Parkfield earthquake. The InSAR dataset consists of eight interferograms from data collected by the Envisat and Radarsat satellites spanning the time of the earthquake and variable amounts of the postseismic period. The two datasets complement each other, with the InSAR providing dense sampling of motion in the range direction of the satellite and the GPS providing more sparse, but three-dimensional measurements of ground motion. The model assumes exponential decay of the postseismic slip with a decay time constant of 0.087 years, determined from time series modeling of continuous GPS and creepmeter data. We find a geodetic moment magnitude of **M** 6.2 for a 1-day coseismic model and M_w 6.1 for the entire postseismic period. The coseismic rupture occurred mainly in two slip asperities; one near the hypocenter and the other 15–20 km north. Postseismic slip occurred on the shallow portions of the fault and near the rupture areas of two **M** 5.0 aftershocks. A comparison of the geodetic slip models with seismic moment estimates suggests that the coseismic moment release of the Parkfield earthquake is as little as 25% of the total. This underlines the importance of aseismic slip in the slip budget for the Parkfield segment.

Online material: Complete data tables and supplemental tables.

Introduction

The 28 September 2004 **M** 6.0 Parkfield earthquake was the long delayed fulfillment of the Parkfield Earthquake Prediction Experiment (Bakun *et al.*, 2005; Bakun and Lindh, 1985; Langbein *et al.*, 2005). Among the goals of the experiment was the desire to study a single event in great detail in order to gain a better general understanding of earthquake processes. To that end, this short segment of the San Andreas fault (SAF) became one of the best-instrumented locations in the world, and the 2004 earthquake has produced copious amounts of data. The years since the original prediction have seen the advent of space-based geodesy; both global positioning system (GPS) and interferometric synthetic aperture radar (InSAR) data can now be added to the wealth of information on this historic earthquake. Here, we use space-based geodetic data to constrain a model of the coseismic and postseismic slip associated with the 2004 Parkfield earthquake. We examine the relationship between these two periods of the earthquake cycle, their relationship to aftershocks, and the extent and importance of aseismic slip.

*Present address: U.S. Geological Survey, 345 Middlefield Road, MS 977, Menlo Park, California 94025.

In some ways, the Parkfield segment of the SAF is a unique environment. The town of Parkfield lies at the southern end of the creeping section of the SAF; a ~100-km-long section where creep rates approach ~3 cm/yr (Burford and Harsh, 1980; Titus *et al.*, 2006). To the south, the SAF interface is locked and last slipped during the 1857 Fort Tejon earthquake (Sieh, 1978). The Parkfield segment forms the transition zone between these two behavioral extremes. It exhibits mixed mechanical behavior; creep continues at the surface, but one or more locked asperities exist at midseismogenic depths (Harris and Segall, 1987; Murray *et al.*, 2001). In this setting, aseismic slip comprises a significant portion of the slip budget and may even regulate the occurrence of seismic events (Gao *et al.*, 2000).

Datasets

It is highly advantageous to combine GPS-derived displacements with InSAR data. InSAR range-change measurements reflect a mixture of vertical and horizontal deformation of unknown ratio, whereas GPS data provides three-dimensional (3D) displacement measurements. InSAR is

limited in its ability to resolve long-wavelength deformation because of uncertainties in the satellite orbit parameters, while GPS has no such limitation. Furthermore, continuous GPS provides dense time sampling that is unavailable using InSAR alone because of the approximate monthly orbit cycle of the satellite. The prime strength of InSAR is its dense spatial coverage; a typical Envisat interferogram has a sample spacing of 80 m (after averaging 4 × 20 samples, or looks). By combining these two complementary datasets, the model inversion for slip on the coseismic rupture exploits the strengths of each.

Interferometric Synthetic Aperture Radar (InSAR)

An interferogram measures the difference in phase between the returning, backscattered radar waves from two separate passes of a radar satellite. The phase difference represents net movement of the ground relative to the satellite (in the radar line-of-sight) during the time spanned by the interferometric pair, usually modified to some extent by other effects (Bürgmann, *et al.*, 2000). The phase difference is measured modulo 2π radians, and one such progression (called a fringe) is equivalent to ground motion of half the radar wavelength (2.8 cm for the Envisat and Radarsat satellites). The discontinuous map of phase differences is unwrapped to form a continuous map of the change in distance between the satellite and the scatterers on the ground (range change).

Twenty-three interferograms (Ⓔ Table S1 in the electronic edition of BSSA) span the coseismic and portions of the postseismic periods. We used data from Envisat imaging beam I2 and Radarsat-1 standard beam S1, both of which have a line of sight to the right of the orbit track (right-looking) and an incidence angle with the Earth's surface at the center of the synthetic aperture rador (SAR) swath of about 23° from the vertical. We include data from both ascending orbit tracks (heading of 346°) and descending tracks (heading of 194°). As a consequence of the geometry of the InSAR line-of-sight, the range-change measurement is most sensitive to vertical motion, less sensitive to east–west motion, and least sensitive to north–south motion.

The spatial sampling of the full-resolution interferograms from Envisat beam I2 and Radarsat-1 beam S1 is about 20 × 4 m on the ground (with the higher resolution in the along-track direction). Because the signal coherence in the Parkfield area is low, we averaged the InSAR data in both the cross-track and along-track directions, giving a total number of samples averaged (called looks) of 4 × 20 (resulting in ~80-m spacing) or 8 × 40 (Table 1).

The interferograms were processed using Roi_pac, developed at JPL/Caltech, and unwrapped using the Snaphu unwrapper (Chen and Zebker, 2001). The Parkfield earthquake was not large, and the deformation from this earthquake produced only 1–2 fringes (3–6 cm) of range change. Many of the interferograms contain noise with apparent range change of nearly the same magnitude as the signal from the earthquake. Identifying the source and amount of noise in each interferogram informed our decision on which to include in our joint inversion (see following section). Six Envisat and two Radarsat interferograms were chosen for modeling the earthquake (Table 1, Figs. 1 and 2).

Atmospheric Delay. Nearly all repeat-pass interferograms suffer from contamination of the desired signal with atmospheric delay errors (Zebker *et al.*, 1997). Atmospheric delay errors occur when water in the troposphere or density changes in the ionosphere slow down the travel time of the radar wave in one of the two scenes in the interferometric pair, causing an apparent change in distance. These errors are generally identifiable as long wavelength patterns or blobs of range change. For this work, some areas with atmospheric delay errors can be avoided because the location and basic pattern of the target signal is known. Two patches of range change to the east and southeast of Parkfield in interferogram E are not near the SAF, nor do they have any other discernible tectonic origin, and they are interpreted to be atmospheric delay error (dashed circles in Fig. 1e). Also, in interferograms B, C, and F, patches of range change to the northwest of Parkfield, in the creeping section of the SAF, are interpreted to be atmospheric delay errors (dashed circles in Fig. 1b,c,f).

Groundwater-Induced Vertical Motion. For the purposes of studying earthquakes or other tectonic processes, groundwater-induced vertical motion is also a source of noise. Subsidence or rebound due to variations in groundwater levels occur in many areas and can have seasonal cycles and long-term components (Amelung *et al.*, 1999; Schmidt and Bürgmann, 2003). All of the interferograms contain the southern portion of the Salinas basin including the Paso Robles subunit, just southwest of Parkfield (white circles in Fig. 1a and Fig. 2a). In 1997, a seasonal change in groundwater levels of 60 ft. in the Paso Robles subunit produced 6 cm of vertical ground motion (Valentine *et al.*, 2001), an amount that is similar to the range change produced by the Parkfield earthquake. Small bulls-eye-shaped range-change patterns in the Paso Robles subunit are apparent in all the interferograms but are most obvious in interferogram A (Fig. 1a). Interferogram A also exhibits an area of range-change increase to the northwest that we interpret to be due to subsidence of the greater Salinas basin.

Petroleum and gas withdrawal from shallow reservoirs can also cause rapid ground subsidence, including at the Lost Hills oil field at the southeast corner of Interferograms A and E (black circles in Fig. 1a,e) (Fielding *et al.*, 1998). This intense deformation is far enough away from the Parkfield earthquake that it is outside the area used in our analysis.

The 22 December 2003 San Simeon Earthquake. The Parkfield earthquake occurred less than a year after the M_w 6.5 San Simeon earthquake and about 50 km to the west. Southern California Integrated GPS Network (SCIGN) con-

Table 1
Interferograms Used in Joint Inversion

Interferogram Letter	Scene ID*	Start Date (mm/dd/yy)	End Date (mm/dd/yy)	Perpendicular Baseline (m)	Time Span (years)	No. of Looks
A	Envisat A435/711	3/7/03	9/30/04	217	1.57	4 × 20
B	Envisat D027/2871–2889	4/14/04	10/6/04	68	0.48	4 × 20
C	Envisat D027/2871–2889	5/19/04	10/6/04	−50	0.38	4 × 20
D	Envisat A206/711	9/14/04	11/23/04	57	0.19	4 × 20
E	Envisat A435/711	8/26/04	12/9/04	79	0.29	4 × 20
F	Envisat D027/2871–2889	6/23/04	12/15/04	−54	0.48	4 × 20
G	Radarsat A 45012–46727	6/19/04	10/17/04	120	0.33	4 × 20
H	Radarsat A 45012–47756	6/19/04	12/28/04	40	0.53	8 × 40

*Envisat scenes are identified by track/frame numbers and Radarsat scenes are identified by start-end orbit numbers. A and D refer to ascending or descending orbit track, respectively.

tinuous GPS stations in the Parkfield area show coseismic motion in a westward direction of up to 1 cm from this event (Hardebeck *et al.*, 2004; Ji *et al.*, 2004; Rolandone *et al.*, 2006) (Ⓔ Table S2 in the electronic edition of BSSA). Postseismic deformation following the San Simeon earthquake is indicated by transient motions of six GPS stations in the region, which rapidly decayed in the aftermath of the event (Savage *et al.*, 2005; Rolandone *et al.*, 2006). Rolandone *et al.* (2006) find that the motions are best explained by afterslip in the upper ~3 km of the crust. The continuous GPS sites in the Parkfield area do not reveal significant San Simeon postseismic motion.

Interferogram A is the only interferogram used that also spans the San Simeon event. Estimates for the coseismic displacements from a model of GPS and InSAR data spanning the San Simeon earthquake (Johanson, 2006) were removed from this interferogram. Though the amount of displacement in the Parkfield area from the San Simeon earthquake was significant, the displacement gradient was small and nearly constant. Similarly, the San Simeon postseismic deformation pattern at Parkfield is very small and long wavelength compared with the deformation signal from the Parkfield earthquake. Any remaining residual far-field displacement gradients from the San Simeon event can be compensated for by including a ramp across the interferograms as part of the model parameters (see the Inversion Setup Section).

Interseismic Deformation. The interferograms used here have variable time spans, and each contains a different contribution from the interseismic deformation field. In the Parkfield area, the interseismic deformation field is the result of the combination of strain accumulation on the regional fault system and steady fault creep. The deformation field from strain accumulation can be modeled as slip on large dislocations below the seismogenic portion of the fault (e.g., from 15- to 3000-km depth) and produces a deformation pattern with wavelength of tens to hundreds of kilometers. Interseismic creep, on the other hand, involves slip on the shallow portions of the fault zone and so produces a shorter wavelength deformation pattern. To forward predict and remove the interseismic displacement field from each interferogram and to predict the interseismic velocity of the campaign GPS stations, we use an interseismic slip model from Rolandone *et al.* (2004). Their model is derived from an inversion of continuous and campaign GPS data along the creeping section of the SAF and the northern and southern transition zones. It contains both deep and shallow model fault elements to capture the effects of strain accumulation and aseismic creep.

Unwrapping Errors. Standard algorithms for unwrapping of the interferogram phase assume that the phase varies smoothly. A discontinuity in the deformation pattern and phase, such as at a surface rupture, requires the unwrapping algorithm to estimate by how many multiples of 2π the phase of the two sides are separated. To facilitate this, it is sometimes necessary to subtract an *a priori* model of the deformation during the time spanned by the interferogram. Subtracting the phase predicted by a model reduces the phase gradients and mitigates unwrapping errors near the surface rupture.

We applied an *a priori* model to aid the unwrapping of interferograms D, E, and F (Table 1). Displacements of continuous GPS sites were estimated for times matching the time spans of the interferograms and including both coseismic and postseismic motions. The estimated displacements were inverted for right-lateral strike slip on a distributed slip model with geometry identical to that described subsequently for the joint inversion. Predicted range changes from the model for each interferogram were subtracted before unwrapping and added back in afterward.

Including these models facilitated successful unwrapping across the SAF zone; however, the Parkfield earthquake involved surface slip on two subparallel strands ~2 km apart. The Southwest Fracture Zone (SWFZ) slipped coseismically at the surface, while the main trace of the SAF exhibited enhanced postseismic creep (Langbein, *et al.*, 2005, 2006). The GPS data used to create the *a priori* model are not dense enough to tightly constrain slip on both strands, so our model includes only a single fault plane at depth and at the surface (see the Model Geometry Section). The un-

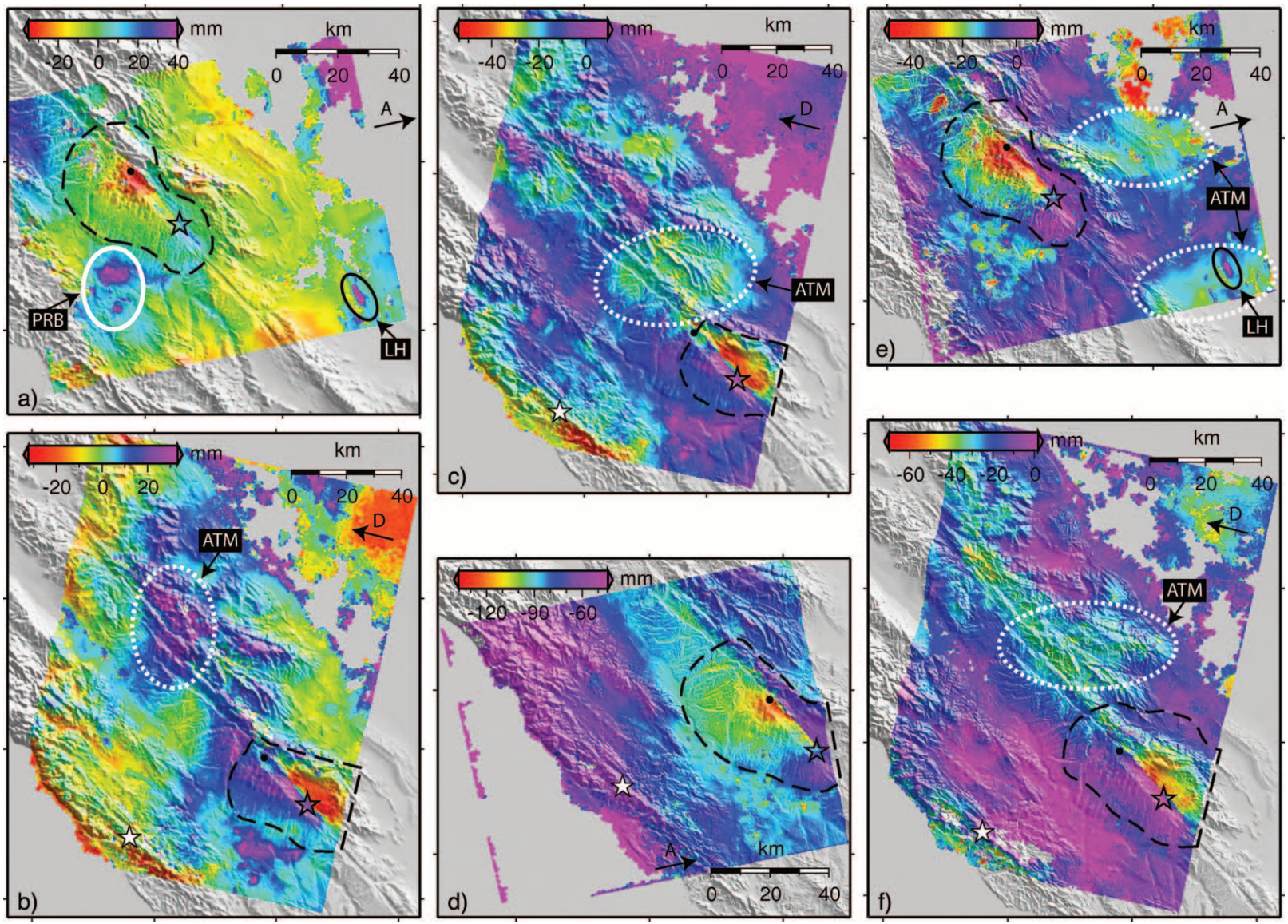

Figure 1. Envisat interferograms (a) 7 March 2003 to 30 September 2004; (b) 14 April 2004 to 6 October 2004; (c) 19 May 2004 to 6 October 2004; (d) 14 September 2004 to 23 November 2004; (e) 28 August 2004 to 9 December 2004; (f) 23 June 2004 to 15 December 2004. Black dashed lines indicate cropped area included in model inversions. White dashed circles refer to atmospheric features mentioned in the text (ATM). Solid white circle indicates the Paso Robles subunit of the Salinas basin (PRB) and solid black circles indicate the Lost Hills oil field (LH). Arrows in the upper right corners are in the radar look direction, with A and D referring to ascending and descending tracks, respectively. The black star in all frames is the epicenter of the 2004 Parkfield earthquake, and the white star is the epicenter of the 2003 San Simeon earthquake.

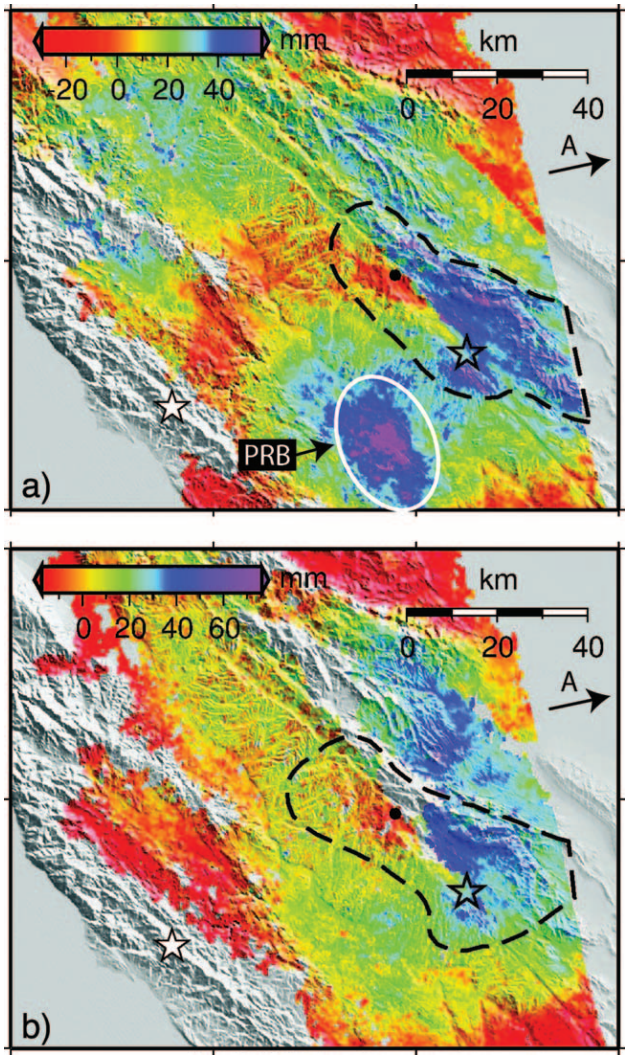

Figure 2. Portions of Radarsat interferograms from ascending swaths covering the Parkfield area. (a) 19 June 2004 to 17 October 2004; (b) 19 June 2004 to 28 December 2004. Black dashed lines indicate cropped area included in model inversions. Solid white circle indicates the Paso Robles subunit of the Salinas basin (PRB). Arrows are the radar look direction, with A referring to the ascending track direction. The black star in both frames is the epicenter of the 2004 Parkfield earthquake and the white star is the epicenter of the 2003 San Simeon earthquake.

wrapping algorithm must decide how to partition the phase change across both strands using information from more smoothly varying parts of the interferogram. This makes the area between the two strands particularly susceptible to unwrapping errors.

Global Positioning System (GPS)

We use GPS-derived horizontal displacements from both campaign and continuous stations (Fig. 3; Ⓔ Table S2 in the electronic edition of BSSA). The campaign data include five stations surveyed by University of California, Berkeley (UCB) and 12 stations surveyed by the U.S. Geological Survey (USGS). The campaign data were processed in daily solutions using GAMIT and combined, using GLOBK/GLORG, with daily solutions from continuous stations in the SCIGN network and the International Global Navigation Satellite System (GNSS) Service (IGS), obtained from the Scripps Orbital and Permanent Array Center (http://sopac.ucsd.edu). Continuous sites from the Earthscope/Plat Boundary Observatory (PBO) network that were installed within a month after the Parkfield earthquake are also included to constrain the postseismic slip.

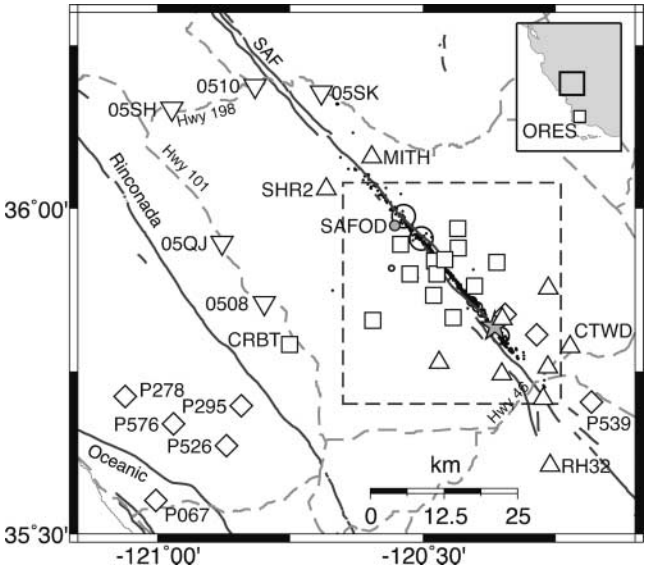

Figure 3. Locations of GPS stations used in this study. Squares are stations in the SCIGN continuous GPS network, diamonds are PBO continuous stations, triangles are campaign stations surveyed by the USGS, and inverted triangles are campaign stations surveyed by UC Berkeley. Solid dark lines are mapped fault traces, and dashed gray lines are major roads. The location of SAFOD is indicated by a gray dot, and the star marks the Parkfield earthquake epicenter. Black circles are double-difference relocated seismicity from Thurber *et al.*, (2006). Dashed box is the spatial extent of Figure 4. Inset map shows location of reference site ORES, with extent of main figure outlined.

Time-Series Modeling. We used time-series modeling to extract the coseismic and postseismic displacements at each GPS station and used these as inputs in the simultaneous slip inversion. The SCIGN continuous GPS stations provided the most complete record of station displacements and were fit by the following model:

$$d_{\text{total}} = c + v_{\text{int}}\, t + d_{\text{ss}} H(t - t_{\text{ss}}) + d_{\text{pk}} H(t - t_{\text{pk}}) \ldots \\ \ldots + d_{\text{ps}}(1 - \exp(-(t - t_{\text{pk}})/\tau)) H(t - t_{\text{pk}}), \quad (1)$$

where $H(t)$ denotes the heavyside step function, occurring at time t. A simplex search method for unconstrained nonlinear optimization was used to find values for a constant (c), the interseismic velocity (v_{int}), offsets at the times of the San Simeon (d_{ss}), and Parkfield (d_{pk}) earthquakes, and the amplitude (d_{ps}) and decay time (τ) of an exponential representing postseismic slip, which minimize the residual sum of squares of the model to the data. We use continuous GPS data from 1 January 2003 to 31 January 2005. The choice of end date was made for two reasons. First of all, the modeled values of τ, and to a lesser degree d_{ps}, were observed to increase for end dates later than 1 February 2005, particularly for stations to the west of the SAF (Ⓔ Fig. S1 and Fig. S2 in the electronic edition of BSSA). With a cutoff date of 31 January 2005, values of τ are consistent on both the east and the west sides of the SAF. Also, values of τ determined separately for the north and east components of the GPS positions were also observed to diverge from each other for end dates later than 1 February 2005. The choice of end date results in similar values of τ for the north and east components when modeled independently, nonetheless a single value of τ was fit to both the north and east components simultaneously. The results of the time-series modeling are shown in Table S2 (Ⓔ available in the electronic edition of BSSA).

Campaign GPS Time-Series Modeling. For the campaign sites, which have sparser time sampling than the continuous sites, subsets of the model parameters in equation (1) were used to model their time series, (Ⓔ Table S2 in the electronic edition of BSSA). Which model parameters were included depended on the observation times of each data source (UCB, USGS, or PBO). For all three, the interseismic slip model described in the Interseismic Deformation section (Rolandone *et al.*, 2004) was used to constrain the interseismic velocities.

The five UCB campaign stations were surveyed three times before the Parkfield earthquake. Two surveys were conducted between the 2003 San Simeon and Parkfield earthquakes, and the offsets from both were estimated. However, we are not able to determine either the amplitude of the postseismic exponential decay or the decay time constant from the UCB campaign GPS data.

Campaign stations surveyed by the USGS did not include observations between the times of the San Simeon and Parkfield earthquakes. In this case, we cannot uniquely determine offsets due to each event. However, many of the stations were surveyed quasi-continuously after the Parkfield earthquake, and so we were able to solve for the amplitude of the postseismic exponential. The decay time constant (τ) was held fixed to the average value of τ (0.087 years) for SCIGN continuous stations and creepmeters as described in the Postseismic Exponential Decay Time Constant section. Five PBO continuous stations installed after the Parkfield earthquake were treated like USGS campaign data in that *a priori* interseismic velocities were used, the postseismic amplitude (d_{ps}) was solved for, and the decay time constant (τ) was fixed to 0.087 years. It was possible to solve for a coseismic offset for three PBO stations installed before the Parkfield earthquake. However, these sites were located ~50 km from the Parkfield rupture area (Fig. 4), and the postseismic amplitude (d_{ps}) was too small to be well determined.

Simultaneous Coseismic and Postseismic Slip Inversion

Earthquake Cycle Effects

All of the datasets used here contain contributions from the coseismic, postseismic, and interseismic periods of the earthquake cycle. Because of the different time spans and sampling of the datasets, they contain different ratios of coseismic, postseismic, and interseismic deformation. This fact is used to our advantage in the model presented here in order to differentiate between coseismic and postseismic slip. The postseismic slip is assumed to evolve with the same exponential decay function as the GPS sites (equation 1), such that the total slip (S_{total}) has the following form:

$$s_{total} = s_{cs} + A_{ps}(1 - e^{-t_{ps}/\tau}), \quad (2)$$

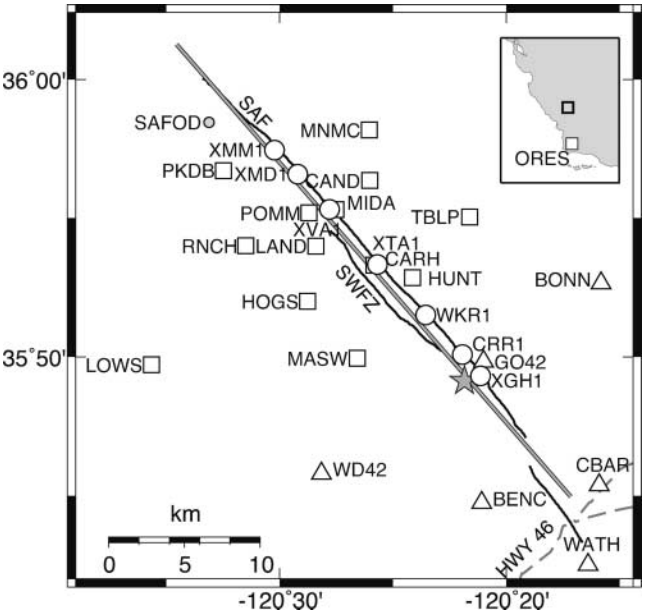

Figure 4. Small-scale location map showing SCIGN continuous GPS stations (squares), USGS creepmeters (circles), and USGS campaign stations (triangles). Solid dark lines are mapped fault traces, and dashed gray line is Highway 46. Gray line outlined in black is the surface projection of the model fault plane. Location of SAFOD is indicated by gray dot, and star is the Parkfield earthquake epicenter. Inset map shows location of reference site ORES, with extent of main figure outlined.

where t_{ps} is the amount of postseismic time spanned by each interferogram; that is, the amount of time between the Parkfield earthquake and the end of the interferogram. Daily time series from continuous GPS stations and USGS creepmeter data were used to constrain the decay time constant (τ) and thereby predict the fraction of the total postseismic deformation field present in each interferogram. A joint inversion was then performed on the InSAR and GPS data for the coseismic slip (s_{cs}) and exponential decay amplitude (A_{ps}, postseismic slip) on each model element. Due to the daily sampling of the GPS time series, our estimate of coseismic slip includes postseismic afterslip of the first day. Studies considering high-rate geodetic time series find that the contribution of afterslip to the deformation during this first day was indeed substantial (Johnson *et al.*, 2006; Langbein *et al.*, 2006). It should be noted that by solving for only A_{ps}, we do not allow the spatial distribution of postseismic slip to change over time. Nonetheless, this approach allows us to take advantage of the number of interferograms available to constrain the model while accounting for the variable time span of each. As a consequence, the estimate of postseismic slip used here is not associated with a finite time span, but reflects the total estimate of cumulative afterslip.

Data Reduction

Because the desired signal in the interferograms is of similar magnitude to the noise sources, as discussed previously, it was necessary to crop the interferograms and include only the Parkfield region in the model inversion (black dashed lines in Fig. 1 and Fig. 2). In addition to not considering areas well outside of the coseismic deformation zone, the cropped regions were chosen to avoid known areas of groundwater-induced vertical motion, such as the Paso Robles subunit, and those areas determined to be heavily contaminated by atmospheric errors. The areas inside the cropped region are not necessarily free of noise sources, but they have a signal-to-noise ratio high enough that the range change related to the Parkfield earthquake will dominate the inversion. The interferograms were further subsampled on a grid with 1-km spacing, where each sample is an average of 16 pixels. This mitigates any correlations that exist between pixels, particularly those introduced by filtering.

Model Geometry

The inversion is restricted to a single, vertical, 40 km $\times$ 15 km plane, which is divided into 300 2 km $\times$ 1 km elements. The 2004 Parkfield earthquake involved slip on multiple surface traces of the SAF as described previously. Although the interferograms include range-change estimates across the entire rupture zone, there is a possibility of unwrapping errors in this area. We therefore choose not to model the complex surface rupture pattern but instead to focus on the slip at depth. The surface projection of our model plane runs between the SAF main trace and the SWFZ (Fig. 4), and the shallow elements in our model reflect the sum of shallow slip across the active strands. The interferogram samples located between the main trace and the SWFZ, and continuous GPS station CARH, were removed from the inversion. An offset between the model plane and the actual surface rupture will tend to cause surface slip to be mapped onto deeper model fault elements. However, the SAF and the SWFZ are within 1–2 km of our model plane, so this effect is expected to be minimal and to be restricted to the top 1–2 km of the model.

One effect of cropping the interferograms is to limit the depth extent over which the inversion can resolve slip. The cropped regions vary between the interferograms, but none include samples more the 30 km from the fault. Slip on fault elements deeper than 20–30 km would trade off heavily with the tilt across the interferograms included in the model parameters. We do not include any dislocations below 15 km in our model geometry. Consequently, the model does not address whether any deep afterslip occurred following the Parkfield earthquake.

Postseismic Exponential Decay Time Constant

The postseismic exponential decay time constant (τ) constrained by data from 12 continuous GPS stations and seven USGS creepmeters (Fig. 4, Ⓔ Tables S2 and S3, available in the electronic edition of BSSA). Figure 5 shows τ as a function of the perpendicular distance from the SAF. The lack of a systematic trend in these values indicates that postseismic slip from deep and shallow depths on the fault did not occur with significantly different decay times. Particularly the fact that the creepmeter estimates are similar to the GPS estimates from further away from the fault indicates that surface creep did not evolve much differently than slip at depth. The decay time constant used in the inversion

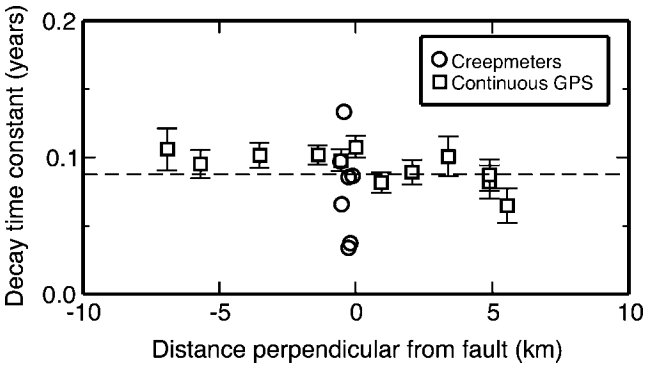

Figure 5. Decay time constants fit to continuous GPS data (squares) and creepmeter data (circles). Dashed line shows average value (0.087 years) used in time-series and slip modeling. Uncertainties for the creepmeter data average 0.003 years; error bars would be about the size of the symbol (Ⓔ Table S3 in the electronic edition of BSSA).

(0.087 years) is the average of the decay time constants determined from the creepmeter records and the selected continuous GPS time series.

Inversion Setup

We invert the eight interferograms and four GPS datasets simultaneously for the coseismic slip and the amplitude of the postseismic exponential decay as follows.

$$\begin{bmatrix} \alpha\mathbf{G}_{s1} & \alpha\mathbf{G}_{s1}(1-\exp(-(t_{ps1}-t_{pk})/\tau)) & \mathbf{xy}_1 \\ \vdots & \vdots & \vdots \\ \alpha\mathbf{G}_{sN} & \alpha\mathbf{G}_{sN}(1-\exp(-(t_{psN}-t_{pk})/\tau)) & \mathbf{xy}_N \\ \mathbf{W}_{gc}\mathbf{G}_{gc} & \mathbf{0} & \mathbf{0} \\ \mathbf{0} & \alpha_{gp}\mathbf{W}_{gp}\mathbf{G}_{gp} & \mathbf{0} \\ \beta_c\nabla^2 & \beta_p\nabla^2 & \mathbf{0} \end{bmatrix}^{-1} \cdot \begin{bmatrix} \alpha\vec{\mathbf{d}}_{s1} \\ \vdots \\ \alpha\vec{\mathbf{d}}_{sN} \\ \mathbf{W}_{gc}\vec{\mathbf{d}}_{pk} \\ \alpha_{gp}\mathbf{W}_{gp}\vec{\mathbf{d}}_{ps} \\ \mathbf{0} \end{bmatrix} = \begin{bmatrix} \vec{\mathbf{s}}_{cs} \\ \vec{\mathbf{A}}_{ps} \\ \vec{\mathbf{t}} \end{bmatrix}, \quad (3)$$

where $\vec{\mathbf{d}}_s$ is the vector of InSAR samples, $\vec{\mathbf{d}}_{pk}$ is the vector of coseismic offsets, and $\vec{\mathbf{d}}_{ps}$ is the vector of amplitudes of the postseismic decay for the GPS data, taken directly from equation (1). $\mathbf{G}_{s1\text{-}N}$, $\mathbf{G}_{gc}$, and $\mathbf{G}_{gp}$ are Green's functions for the InSAR, coseismic GPS, and postseismic GPS data, respectively. The Green's functions are constructed using Okada's equations (Okada, 1985) to relate unit slip on each dislocation to displacements at the surface. $t_{ps1\text{-}N}$ are the ending times of the interferograms (Table 1), and t_{pk} is the time of the Parkfield earthquake.

$\mathbf{W}_{gc}$ and $\mathbf{W}_{gp}$ are the covariance matrices for the coseismic and postseismic GPS data, respectively, used to weight the data in the inversion. The InSAR dataset is weighted in the inversion relative to the GPS through the factor α, which has the effect of scaling the InSAR uncertainties. For this inversion, α is chosen so that the InSAR dataset has twice the weight of the GPS dataset, that is, $\sum_N |\alpha\vec{\mathbf{d}}_{sN}| = 2(|\mathbf{W}_{gc}\vec{\mathbf{d}}_{pk}| + |\alpha_{gp}\mathbf{W}_{gp}\vec{\mathbf{d}}_{ps}|)$. The heavier weight on the InSAR data is because it contains more separate time spans (Table 1), and consequently more information about the postseismic slip evolution. If the full covariance matrix for InSAR data were better known, it could be weighted by its actual uncertainties. Several previous authors have devised schemes for choosing data weights in the absence of complete knowledge of the covariance matrix. These include scaling the datasets relative to the model roughness (Kaverina *et al.*, 2002; Price and Bürgmann 2002) and choosing a weight for one data type that does not severely affect the fit to other data types (e.g., Schmidt *et al.*, 2005). Our choice of α is consistent with the latter scheme; weighting the InSAR data twice as heavily increases the GPS misfit by only 4% and decreases the InSAR misfit by 3% over even weighting. The factor α_{gp} is used to further weight the postseismic GPS data relative to the InSAR data. Because the interferograms are not cleanly separated into coseismic and postseismic portions, the data vectors cannot be used to define the weights. Instead, α_{gp} is chosen such that the ratio of the magnitude of the GPS Green's function to the sum of the magnitudes of the InSAR Green's functions is identical for the coseismic and postseismic models. This ensures that the coseismic and postseismic slip models have the same relative weights of InSAR and GPS data.

The Laplacian operator (∇^2) is used to apply smoothing to the modeled slip and is weighted by β_c and β_p, for the coseismic and postseismic slip models, respectively. The Laplacian operator is constructed to smooth the model toward zero slip at the northwest, southeast, and bottom edges of the model plane. Smoothing weights were chosen to provide a smooth model while not significantly increasing the model misfit, and the results of increasing and decreasing the smoothing are shown in Figure S3 (Ⓔ electronic edition of BSSA). We further constrain the model to allow only right-lateral strike slip by implementing a bounded-value least-squares algorithm to perform the inversion (Stark and Parker, 1995).

$\mathbf{xy}_N$ are the Green's functions relating the interferogram samples to an offset and gradient across the interferogram ($\vec{\mathbf{t}}$). A gradient is typically included in inversions of InSAR data to account for possible errors in the orbit parameters. However, because the interferograms have been cropped to a fraction of their original size, solving for a ramp on the small subset could imply a large phase error in the distant parts of the interferograms that is unrealistic. Nonetheless the ramp terms are included in the inversion to account for long-wavelength noise sources, such as atmospheric water vapor variations or the far-field postseismic transient deformation from the San Simeon earthquake.

Results and Discussion

Figure 6 shows the results of the inversion for coseismic slip and for the total slip amplitude of the postseismic exponential (A_{ps}, postseismic slip). The coseismic slip occurred in two asperities: asperity A is located near the hypocenter and asperity B is 15–20 km northwest of the hypocenter. The postseismic slip has its maximum north of asperity B and deeper on the fault surface (asperity D), near two **M** 5.0 aftershocks and includes another asperity (asperity C) near asperity A. The postseismic slip model also includes enhanced slip in the shallow portions of the fault. In the northwestern half of the model, the coseismic and postseismic slip patterns appear complementary to each other. Asperity B is an area of high slip in the coseismic model, but the same

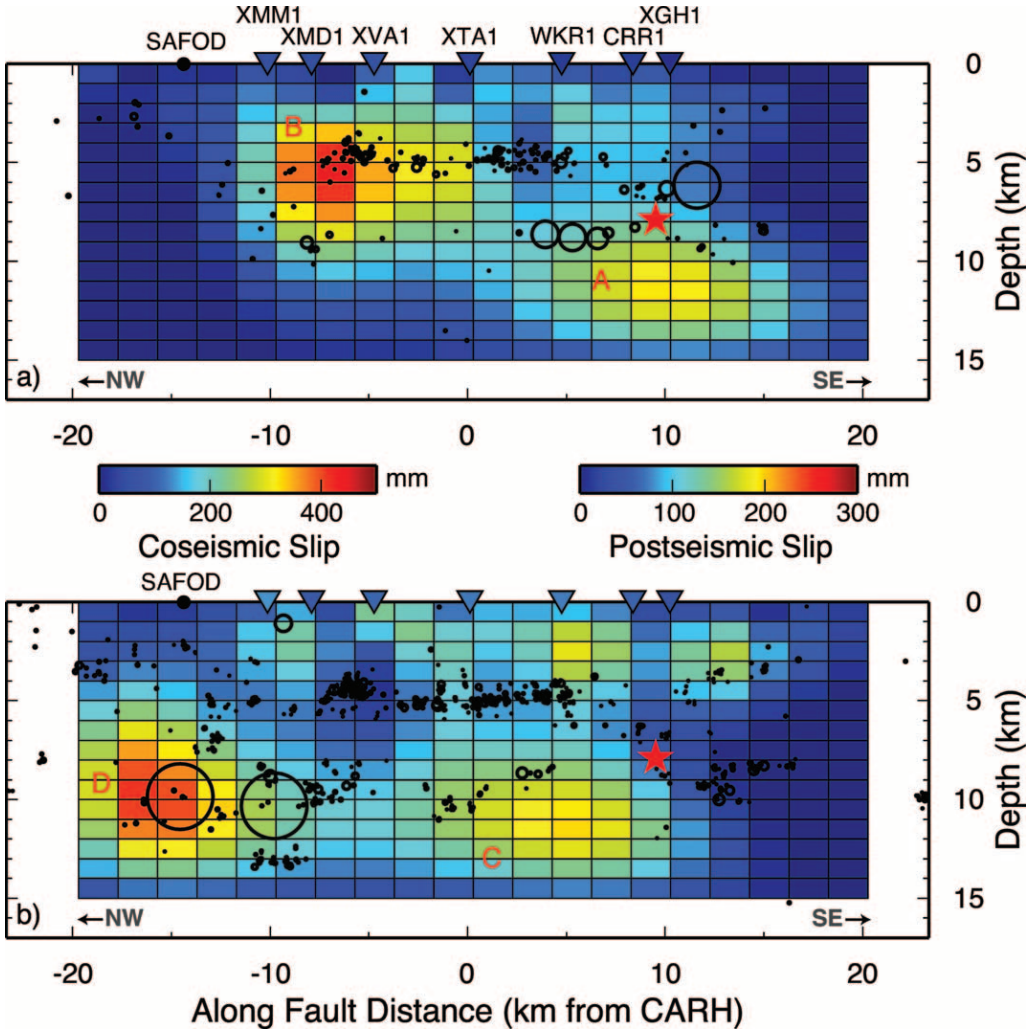

Figure 6. Results of inversion for (a) coseismic slip and (b) postseismic slip. Red stars mark location of earthquake hypocenter. Black circles are double-difference relocated aftershocks (Thurber *et al.*, 2006); symbol size is scaled to actual size of rupture assuming 3 MPa stress drop and circular rupture. The coseismic model is plotted with the first day of aftershocks; the postseismic slip model is plotted with aftershocks from 29 September through 17 November 2004. Letters A, B, C, and D refer to asperities mentioned in the text. Triangles are creepmeter displacements roughly corresponding to the coseismic and postseismic periods (described in more detail in the text), and color coded using the same scale as the slip models.

area experiences little postseismic slip. Similarly, asperity D is located in an area in which no slip was resolved in the coseismic model.

In general the fit to the data is good, with only a few significant residuals (Figs. 7 and 8). Two PBO stations with postseismic estimates are underfit by the postseismic slip model. Observations at these two stations began in November 2004; therefore the total amplitude of the postseismic exponential is not well constrained. Removing these two stations from the inversion reduces the amount of shallow slip south of the epicenter but does not remove it entirely (Ⓔ Fig. S5 in the electronic edition of BSSA). Interferograms D and F have near-fault residuals indicating an overestimate of the shallow slip for these interferograms. This could be due to time-dependent variations in shallow slip, besides the exponential decay, which are not accounted for in our model. It is apparent in Figure 7 that the InSAR residuals and the predicted range change due to postseismic slip have similar magnitudes. This illustrates the importance of using multiple interferograms when the tectonic signal is small.

The inversion was repeated using only the InSAR data and then only the GPS data (Fig. 9). The separate inversions have limited resolution power along different portions of the model where either GPS stations or coherent InSAR data are sparse. In the coseismic model, the pattern of slip in both single-data type inversions is similar and suggests that the

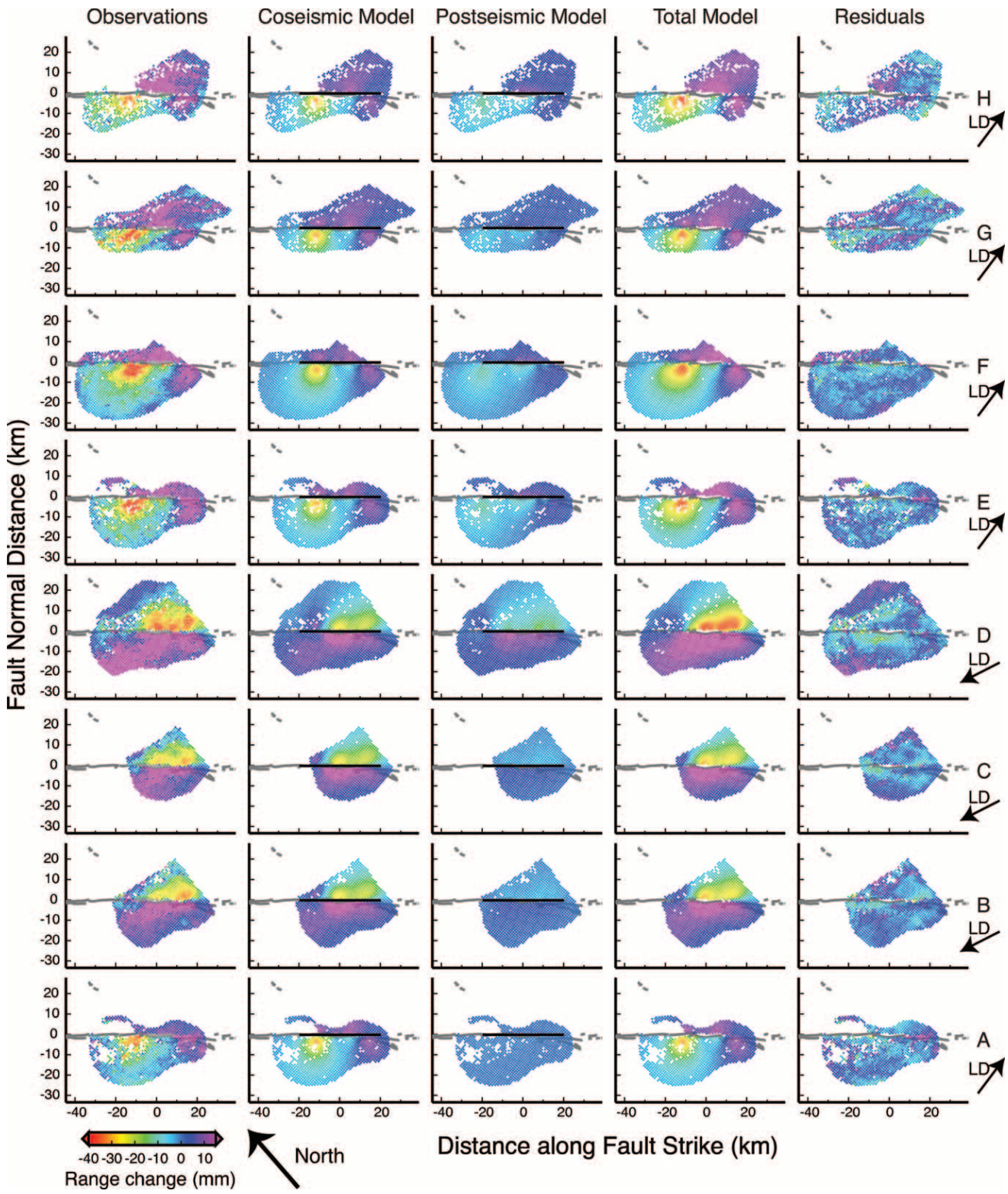

Figure 7. Model fits to InSAR data. Letters refer to interferograms listed in Table 1. LD, look direction, direction of satellite view. Gray colored samples under Observations are those lying between the main SAF and SWFZ, which were removed before modeling. (Ⓔ A high-resolution version of this figure is available as Fig. S4 in the electronic edition of BSSA).

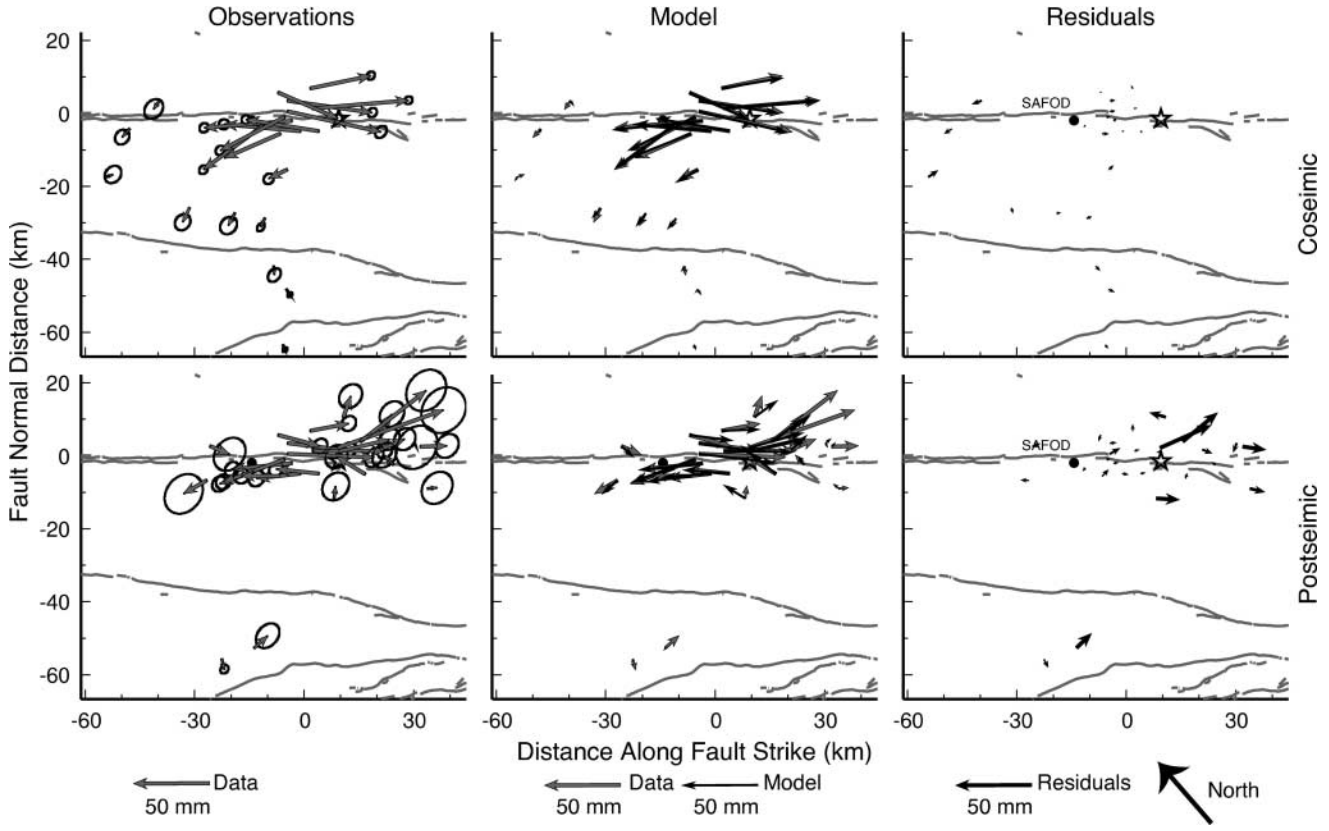

Figure 8. Model fits and residuals for the GPS data. Top row is stations with coseismic estimates (d_{pk} in equation 3) and their fit to the coseismic slip model. The bottom is stations with postseismic amplitudes (d_{ps} in equation 3) and their fit to the postseismic slip model. Displacements are relative to station ORES (Fig. 3). 95% confidence error ellipses are plotted with the observations. Black dot is the location of SAFOD, and the black star is the Parkfield earthquake epicenter.

results found here are not overly sensitive to dataset weighting (α). However, for the postseismic slip models, the GPS-only inversion resolves more shallow slip than the InSAR-only inversion. Though both resolve enhanced postseismic slip north of SAFOD, the inferred slip occurs at different depths; the GPS-only inversion favors shallow slip here, while the InSAR and the joint inversions do not.

Surface Slip

The amount of slip resolved in the topmost row of model elements in the coseismic and postseismic periods is similar to the displacements measured by creepmeters (Fig. 6). Many of the USGS creepmeters went off scale during or just after the Parkfield earthquake and had to be reset by hand. The total fault displacement while the instrument was off scale was measured with a micrometer (Langbein *et al.*, 2006). We plot the displacements from before the earthquake to after the instrument was brought back on scale with the coseismic slip model. Displacements from when the instruments were reset to 31 January 2005 are plotted with the postseismic slip model. Early postseismic slip occurred rapidly in some areas, so we expect the coseismic creepmeter displacements to be an overestimate and the postseismic displacements to be an underestimate. Nonetheless, our model correctly captures the overall magnitude and some of the details of the surface-slip distribution. According to the coseismic model, surface slip continued at low levels north of Middle Mountain up to near the SAFOD. Surface slip in the coseismic model terminates at Gold Hill in the south (creepmeter XGH1), although postseismic surface slip continued for another ~6 km. The extent of surface slip in the models is similar to field observations, where patches of ground breakage were observed from 2 km north of SAFOD and continued until about 5 km south of Gold Hill (Rymer *et al.*, 2006).

Relationship to Aftershocks

Double-difference relocation of Parkfield aftershocks shows that they occurred in streaklike patterns similar to those seen in the background seismicity, including a prominent streak at ~5-km depth (Langbein *et al.*, 2006; Thurber *et al.*, 2006). One interpretation of microseismicity streaks is that they occur at the boundaries of creeping and locked asperities of the fault surface (Nadeau *et al.*, 1995). Thus, the microseismic streak would be expected to bound areas

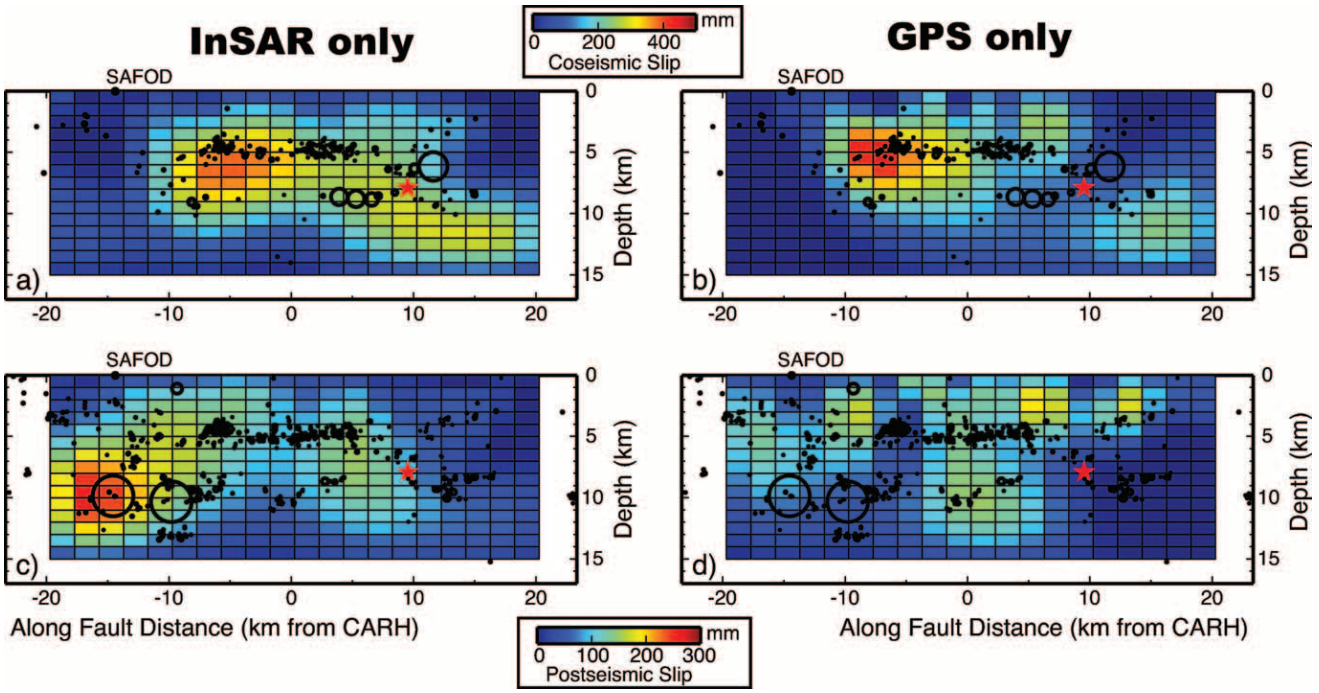

Figure 9. (a), (c) Comparison of inversion using only InSAR data and (b), (d) only GPS data for both the (a), (b) coseismic and (c), (d) postseismic slip models. Compare with Figure 6 for which InSAR data was weighted twice as heavily as GPS data. Annotations are the same as in Figure 6.

of high coseismic slip. The streak of aftershocks at 5-km depth occurs near the top of asperity B (Fig. 6a) and could be interpreted as weakly bounding the asperity. Furthermore, a smaller streak of aftershocks near the hypocenter at 9-km depth lies near the tops of asperities A and C. In the postseismic slip model, much of the shallow slip occurs in the fault region above the 5-km aftershock streak (Fig. 6b).

The area of enhanced postseismic slip to the northwest corresponds with the location of two **M** 5.0 aftershocks that occurred on 29 and 30 September. Assuming a 3 MPa stress drop and circular rupture, these events contributed 13 cm of slip to the postseismic slip model. However, the model indicates as much as 25 cm of slip over a similar area and suggests that significant aseismic slip occurred near the aftershock hypocenters. Our model cannot address the relative timing or spatial association of the aftershocks and the aseismic slip and whether the earthquakes occurred in response to increased creep rates or if they unpinned the fault surface and allowed enhanced creep to take place. Also, because model resolution decreases with depth, the model cannot address whether the areas of the fault that slipped seismically in aftershocks also slipped aseismically.

Seismic versus Aseismic Moment Release

The model yields a moment estimate of 2.16×10^{18} N m (M_w 6.2) for the coseismic period and 1.63×10^{18} N m (M_w 6.1) for the postseismic period, using a value of 30 GPa for rigidity. Because the postseismic slip model is derived from the amplitudes of the postseismic exponential decay, the postseismic moment magnitude is not associated with any particular time span but is an estimate for the entire postseismic period. The total moment for both periods is 3.79×10^{18} N m (M_w 6.3).

Our coseismic moment magnitude is larger than seismic estimates of M_w 6.0 ($M_0 = 9.4 \times 10^{17} - 1.1 \times 10^{18}$ N m) (Langbein *et al.*, 2005). Langbein *et al.* (2006) and Murray and Langbein (2006) used 1-Hz GPS data, together with strainmeter data, to constrain models of coseismic slip with moments of 1.1×10^{18} N m and 1.3×10^{18} N m, respectively. Our larger estimate could be due to aseismic slip from early in the postseismic period being included in our coseismic model. If the coseismic moment were between 9.4×10^{17} and 1.3×10^{18}, then 40%–55% of the slip in our 1-day coseismic model would be aseismic. Both coseismic models from 1-Hz data have their peak slip ~15 km north of the hypocenter, similar to its location in our model (asperity B). However, neither includes as much slip near the hypocenter (asperity A) as our model, which suggests that this slip asperity may be predominantly composed of rapid afterslip.

Rapid and copious postseismic slip was also observed following the 1966 Parkfield event (Smith and Wyss, 1968) and for several subduction zone earthquakes (Heki *et al.*, 1997; Bürgmann *et al.*, 2001). The profusion of postseismic, aseismic slip at these locations is almost certainly related to

their transitional nature (including both locked and creeping fault areas) and the juxtaposition of velocity-strengthening and velocity-weakening fault materials. The regions of enhanced postseismic slip occur near the edges of the coseismic slip in areas that would have experienced increased stress from the coseismic rupture. This is consistent with the view that velocity-strengthening segments of the SAF experienced transient accelerated slip in response to the Parkfield stick-slip event (Marone *et al.*, 1991; Hearn *et al.*, 2002; Johnson *et al.*, 2006). In fact, geodetic estimates of combined coseismic and early postseismic moment release for the 1934 and 1966 Parkfield earthquakes have consistently obtained estimates in the range of M_w 6.3–6.6 (Segall and Harris, 1987; Segall and Du, 1993; Murray and Segall, 2002; Murray and Langbein, 2006). The similarity of our results for the 2004 Parkfield earthquake to those for the earlier events is evidence that these are to some extent characteristic earthquakes; however, Segall and Du (1993) and Murray and Langbein (2006) find significant differences in the details of the slip distributions. Large amounts of postseismic slip appear to be characteristic of the Parkfield area and underscore the need to explicitly consider aseismic slip in any time-predictable model of earthquake occurrence in transition zones.

Conclusions

We simultaneously inverted InSAR and GPS data for coseismic (event plus 1-day afterslip) and postseismic slip from the 2004 Parkfield earthquake. The model indicates that coseismic slip occurred as two asperities, with the larger being northwest of the hypocenter by 15 km. For the postseismic period, the model identifies a deep slip patch near the location of two **M** 5.0 aftershocks and another near the hypocenter. The slip model suggests that a streak of microseismicity at 5-km depth forms a dividing line between coseismic slip below and postseismic slip above. In general, postseismic slip is enhanced in the areas directly surrounding the coseismic rupture. The model indicates that surface slip extended from ~6 km south of Gold Hill to near SAFOD and occurred mostly during the postseismic period. We obtain a moment magnitude estimate of M_w 6.2 for the coseismic rupture plus 1-day of slip and M_w 6.1 for the subsequent postseismic period. The difference between our coseismic estimate and seismic and high-frequency GPS-derived moment magnitudes of M_w 6.0 implies that our coseismic model contains substantial early afterslip and that 66%–75% of the total (coseismic and postseismic) moment release associated with the Parkfield earthquake occurred aseismically.

Acknowledgments

The authors would like to thank Sue Owen, Ken Hudnut, and Ramón Arrowsmith for their informed and insightful reviews of this manuscript. Envisat SAR data were provided to the WInSAR Consortium by the European Space Agency (ESA) under Project Cat1-2525, and also provided under Project AOE-668. Original Envisat data are copyrighted by ESA. SAR data collected by the Radarsat satellite of the Canadian Space Agency were processed by the Alaska Satellite Facility (ASF). This work was supported in part by National Science Foundation (NSF) Grant EAR-0337308 and the Southern California Earthquake Center (SCEC). SCEC is funded by NSF Cooperative Agreement EAR-0106924 and USGS Cooperative Agreement 02HQAG0008. Part of this research was performed at the Jet Propulsion Laboratory, California Institute of Technology, under contract with the National Aeronautics and Space Administration. This is SCEC Contribution No. 990 and BSL Contribution No. 06-06.

References

Amelung, F., D. L. Galloway, J. W. Bell, H. A. Zebker, and R. J. Laczniak (1999). Sensing the ups and downs of Las Vegas; InSAR reveals structural control of land subsidence and aquifer-system deformation, *Geology* **27,** no. 6, 483–486.

Bakun, W. H., and A. G. Lindh (1985). The Parkfield, California, earthquake prediction experiment, *Science* **229,** no. 4714, 619–624.

Bakun, W. H., B. Aagaard, B. Dost, W. L. Ellsworth, J. L. Hardebeck, R. A. Harris, C. Ji, M. J. S. Johnston, J. Langbein, J. J. Lienkaemper, A. J. Michael, J. R. Murray, R. M. Nadeau, P. A. Reasenberg, M. S. Reichle, E. A. Roeloffs, A. Shakal, R. W. Simpson, and F. Waldhauser (2005). Implications for prediction and hazard assessment from the 2004 Parkfield earthquake, *Nature* **437,** no. 7061, 969–974.

Burford, R. O., and P. W. Harsh (1980). Slip on the San Andreas fault in central California from alignment array surveys, *Bull. Seism.* Soc. Am. **70,** no. 4, 1233–1261.

Bürgmann, R., M. G. Kogan, V. E. Levin, C. H. Scholz, R. W. King, and G. M. Steblov (2001). Rapid aseismic moment release following the 5 December, 1997 Kronotsky, Kamchatka, earthquake, *Geophys. Res. Lett.* **28,** no. 7, 1331–1334.

Bürgmann, R., P. A. Rosen, and E. J. Fielding (2000). Synthetic aperture radar interferometry to measure Earth's surface topography and its deformation, *Annu. Rev. Earth Planet. Sci.* **28,** 169–209.

Chen, C. W., and H. A. Zebker (2001). Two-dimensional phase unwrapping with use of statistical models for cost functions in nonlinear optimization, *J. Opt. Soc. Am.* **18,** no. 2, 338–351.

Fielding, E. J., R. G. Bloom, and R. M. Goldstein (1998). Rapid subsidence over oil fields measured by SAR interferometry, *Geophys. Res. Lett.* **25,** no. 17, 3215–3218.

Gao, S. S., P. G. Silver, and A. T. Linde (2000). Analysis of deformation data at Parkfield, California: detection of a long-term strain transient, *J. Geophys. Res.* **105,** no. B2, 2955–2968.

Hardebeck, J. L., J. Boatwright, D. Dreger, R. Goel, V. Graizer, K. Hudnut, C. Ji, L. Jones, J. Langbein, J. Lin, E. Roeloffs, R. Simpson, K. Stark, R. Stein, and J. C. Tinsley (2004). Preliminary report on the 22 December 2003, M 6.5 San Simeon, California earthquake, *Seism. Res. Lett.* **75,** no. 2, 155–172.

Harris, R. A., and P. Segall (1987). Detection of a locked zone at depth on the Parkfield, California, segment of the San Andreas fault, *J. Geophys. Res.* **92,** no. B8, 7945–7962.

Hearn, E. H., R. Bürgmann, and R. E. Reilinger (2002). Dynamics of Izmit earthquake postseismic deformation and loading of the Duzce earthquake hypocenter, *Bull. Seism. Soc.* Am. **92,** no. 1, 172–193.

Heki, K., S.-i. Miyazaki, and H. Tsuji (1997). Silent fault slip following an interplate thrust earthquake at the Japan Trench, *Nature* **386,** no. 6625, 595–598.

Ji, C., K. L. Larson, Y. Tan, K. W. Hudnut, and K. Choi (2004). Slip history of 2003 San Simeon earthquake constrained by combining 1-Hz GPS, strong motion, and teleseismic data, *Geophys. Res. Lett.* **31,** no. L17608, doi 10.1029/2004GL020448.

Johanson, I. A. (2006). Slip characteristics of San Andreas fault transition zone segments, *Ph.D. Thesis,* University of California, Berkeley, 117 pp.

Johnson, K., R. Bürgmann, and K. Larson (2006). Frictional afterslip following the 2004 Parkfield, California, earthquake, *Bull. Seism. Soc. Am.* **96,** no. 4B, S321–S338.

Kaverina, A., D. Dreger, and E. Price (2002). The combined inversion of seismic and geodetic data for the source process of the 16 October 1999 M_w 7.1 Hector Mine, California, earthquake, *Bull. Seism. Soc. Am.* **92,** no. 4, 1266–1280.

Langbein, J., R. Borcherdt, D. Dreger, J. Fletcher, J. L. Hardebeck, M. Hellweg, C. Ji, M. Johnston, J. R. Murray, and R. Nadeau (2005). Preliminary Report on the 28 September 2004, M 6.0 Parkfield, California Earthquake, *Seism. Res. Lett.* **76,** no. 1, 10–26.

Langbein, J., J. Murray, and H. A. Snyder (2006). Coseismic and initial postseismic deformation from the 2004 Parkfield, California, earthquake, observed by Global Positioning System, creepmeters, and borehole strainmeters, *Bull. Seism. Soc. Am.* **96,** no. 4B, S304–S320.

Marone, C. J., C. H. Scholz, and R. Bilham (1991). On the mechanics of earthquake afterslip, *J. Geophys. Res.* **96,** no. B5, 8441–8452.

Murray, J., and J. Langbein (2006). Slip on the San Andreas fault at Parkfield, California, over two earthquake cycles and the implications for seismic hazard, *Bull. Seism. Soc. Am.* **96,** no. 4B, S283–S303.

Murray, J., and P. Segall (2002). Testing time-predictable earthquake recurrence by direct measurement of strain accumulation and release, *Nature* **419,** no. 6904, 287–291.

Murray, J. R., P. Segall, P. Cervelli, W. Prescott, and J. Svarc (2001). Inversion of GPS data for spatially variable slip-rate on the San Andreas fault near Parkfield, California, *Geophys. Res. Lett.* **28,** no. 2, 359–362.

Nadeau, R. M., W. Foxall, and T. V. McEvilly (1995). Clustering and periodic recurrence of microearthquakes on the San Andreas fault at Parkfield, California, *Science* **267,** no. 5197, 503–507.

Okada, Y. (1985). Surface deformation due to shear and tensile faults in a half-space, *Bull. Seism. Soc. Am.* **75,** no. 4, 1135–1154.

Price, E. J., and R. Bürgmann (2002). Interactions between the Landers and Hector Mine, California, earthquakes from space geodesy, boundary element modeling, and time-dependent friction, *Bull. Seism.* Soc. Am. **92,** no. 4, 1450–1469.

Rolandone, F., D. Dreger, M. Murray, and R. Bürgmann (2006). Coseismic slip distribution of the 2003 M_w 6.6 San Simeon earthquake, California, determined from GPS measurements and seismic waveforms data, *Geophys. Res. Lett.* **33,** (in press).

Rolandone, F., I. Johanson, R. Bürgmann, and D. Agnew (2004). Variation in aseismic slip and fault normal strain along the creeping section of the San Andreas fault from GPS, InSAR and trilateration data, *EOS Trans. AGU* **85,** G32A-05.

Rymer, M. J., J. C. Tinsley III, J. A. Treiman, J R. Arrowsmith, K. B. Clahan, A. M. Rosinski, W. A. Bryant, H. A. Snyder, G. S. Fuis, N. A. Toké, and G. W. Bawden (2006). Surface fault slip associated with the 2004 Parkfield, California, earthquake, *Bull. Seism. Soc. Am.* **96,** no. 4B, S11–S27.

Savage, J. C., J. L. Svarc, and S. Yu (2005). Postseismic relaxation and transient creep, *J. Geophys. Res.* **110,** no. B11402, doi 10.1029/2005JB003687.

Schmidt, D. A., and R. Bürgmann (2003). Time-dependent land uplift and subsidence in the Santa Clara valley, California, from a large interferometric synthetic aperture radar data set, *J. Geophys. Res.* **108,** no. B9, 2416.

Schmidt, D. A., R. Bürgmann, R. M. Nadeau, and M. d'Alessio (2005). Distribution of aseismic slip rate on the Hayward fault inferred from seismic and geodetic data, *J. Geophys. Res.* **110,** no. B08406, doi 10.1029/2004JB003397.

Scripps Orbit and Permanent Array Centor, Insitute of Geophysics and Planetory Physics, University of California, San Diego, http://sopac.ussd.edu. (last accessed July 2006).

Segall, P., and Y. Du (1993). How similar were the 1934 and 1966 Parkfield earthquakes? *J. Geophys. Res.* **98,** no. B3, 4527–4538.

Segall, P., and R. A. Harris (1987). Earthquake deformation cycle on the San Andreas fault near Parkfield, California, *J. Geophys. Res.* **92,** no. B10, 10,511–10,525.

Sieh, K. E. (1978). Slip along the San Andreas fault associated with the great 1857 earthquake, *Bull. Seism. Soc. Am.* **68,** no. 5, 1421–1447.

Smith, S. W., and M. Wyss (1968). Displacement on the San Andreas fault subsequent to the 1966 Parkfield earthquake, *Bull. Seism. Soc. Am.* **58,** no. 6, 1955–1973.

Stark, P. B., and R. L. Parker (1995). Bounded-variable least-squares—an algorithm and applications, *Computation Stat.* **10,** no. 2, 129–141.

Thurber, C., H. Zhang, F. Waldhauser, J. Hardebeck, A. Michael, and D. Eberhart-Phillips (2006). Three-dimensional compressional wavespeed model, earthquake relocations, and focal mechanisms for the Parkfield, California, region, *Bull. Seism. Soc. Am.* **96,** no. 4B, S38–S49.

Titus, S. J., C. DeMets, and B. Tikoff (2006). Thirty-five-year creep rates for the creeping segment of the San Andreas fault and the effects of the 2004 Parkfield earthquake: constraints from alignment arrays, continuous Global Positioning System, and creepmeters, *Bull. Seism. Soc. Am.* **96,** no. 4B, S250–S268.

Valentine, D. W., J. N. Densmore, D. L. Galloway, and F. Amelung (2001). Use of InSAR to identify land-surface displacements caused by aquifer-system compaction in the Paso Robles Area, San Luis Obispo County, California, March to August 1997, *U.S. Geol. Surv. Open-File Rept. 00-447.*

Zebker, H. A., P. A. Rosen, and S. Hensley (1997). Atmospheric effects in interferometric synthetic aperture radar surface deformation and topographic maps, *J. Geophys. Res.* **102,** no. B4, 7547–7563.

University of California, Berkeley
Berkeley Seismological Laboratory
215 McCone Hall
Berkeley, California 94027
ingrid@seismo.berkeley.edu
(I.A.J., R.B.)

Jet Propulsion Laboratory/California Institute of Technology
4800 Oak Grove Drive
Pasadena, California 91109
(E.J.F.)

Université Pierre et Marie Curie—Paris VI
Laboratoire de Tectonique—CNRS UMR7072
Barre 46-45 Niveau 2—Case 129
4, Place Jussieu F-75252, Paris Cedex 05, France
(F.R.)

Manuscript received 17 September 2005.